Synthesis and transport properties of superconducting thin films of $K_{0.33}WO_3$: T_c reduction due to disorder

Phillip M. Wu,[1] Chris Hart,[1,2] Katherine Luna,[1] Ko Munakata,[1] Akio Tsukada,[1]
Subhash H. Risbud,[2] T. H. Geballe,[1] and M. R. Beasley[1]
[1]*Department of Applied Physics, Stanford University, Stanford, California 94305, USA*
and Geballe Laboratory for Advanced Materials, Stanford University, Stanford, California 94305, USA
[2]*Materials Science and Engineering Program, University of California, Davis, California 95616, USA*
(Received 15 March 2014; revised manuscript received 17 April 2014; published 2 May 2014)

Via a two-step deposition and post-annealing procedure, K-doped WO_3 thin films with reproducible transport properties are obtained. We observe a larger critical field H_{c2} along the c axis, consistent with the picture of the Fermi surface containing one-dimensional bands along this direction. Reducing the film thickness results in a superconductor to insulator transition. Scanning electron microscopy (SEM) images show that KWO_3 crystallites become less connected as the deposition time is reduced, providing a microscopic explanation for the transport behavior. In the superconducting films, a resistive anomaly is observed similar to bulk crystals, with a characteristic temperature that shifts lower with decreasing film thickness. The competing electronic effects manifest as a suppression of the density of states at the Fermi level, observed using point contact tunneling spectroscopy, demonstrating that disorder-induced increased Coulomb interactions are present. Using the theory of Belitz for the reduction of T_c due to disorder, we can infer that the film with the highest observed T_c has a relatively large disorder dependent electron-phonon interaction parameter $\sim$1.2. Understanding microscopically why certain films display higher T_c will aid in the search for the trace high-T_c superconducting anomalies observed in lightly surface doped bronzes.

DOI: 10.1103/PhysRevB.89.184501 PACS number(s): 74.25.F−, 74.62.En, 74.78.−w

I. INTRODUCTION

The observation of apparent trace high-T_c superconducting anomalies in lightly surface doped tungsten bronzes [1–3] above liquid nitrogen temperatures has renewed interest in this material system. Localized superconducting islands with diamagnetic transitions at these high temperatures were reported to nucleate on the surface, with a small areal fraction much below the percolation threshold. These studies point to the importance of understanding superconductivity at surfaces and interfaces involving the tungsten bronzes. Possible origins of the purported superconductivity include metastable phases, intrinsic properties of oxide interfaces, the recently proposed proximity effect mechanism of high-temperature superconductivity [4] and the older proposal of Ginzburg that superconductivity could arise at the interface between a metal and a dielectric due to the polarizability of the dielectric (the so-called excitonic mechanism) [5]. Finally, we note that the mechanism of the superconductivity in bulk doped tungsten bronzes is not indisputably established.

Chemically doped bulk WO_3 tungsten bronzes (A_xWO_3, where A = Na, K, Rb, Cs), have a three-dimensional (3D) WO_3 lattice with corner-sharing WO_6 octahedra, where the alkali-metal cation resides in the octahedral channels. When Na-doped, the structure is closer to an ideal perovskite ABO_3 [1,3,6], while doping with larger alkali ions such as K, Rb, and Cs leads to a hexagonal lattice [7–12]. Hexagonal doped bronzes are structurally stable in the dopant concentration range of $0.15 < x < 0.33$. At 1/3 doping, all alkali atom sites in the hexagonal tunnels are occupied.

The transport properties of bulk A_xWO_3 are sensitive to both the alkali doping and oxygen concentration [9]. Superconductivity is found for all stable Cs doping levels, with T_c increasing as Cs concentration is reduced until phase stability is breached. In contrast, a superconducting transition is observed only for $x > 0.3$ and $x < 0.2$ in the K- and Rb-doped bronzes [7,8,10]. In addition, these systems exhibit anomalies in the electrical resistivity at high temperature not found in the Cs system. The characteristic temperature of the anomaly, T_B, exhibits a maximum at $x = 0.25$, where superconductivity is no longer found. These features are attributed to several possibilities: ordering of the alkali vacancies [11,12], alkali concentration dependent crystallographic phase change, and formation of a charge density wave (CDW) instability along the c axis [13].

In light of all this complexity and in order to bring modern surface analytical tools (e.g., ARPES, STM, scanning transport, and magnetic local probes) to bear on the study of the superconducting anomalies noted above, we seek to develop deposition procedures to produce thin films of alkali-doped tungsten bronzes. Thin films also permit more systematic surface doping studies. Here, we report our efforts on hexagonal K-doped WO_3 thin films. We have investigated and found an annealing procedure during K-doped WO_3 film synthesis to obtain reliable transport results. In this paper, we report a study of the deposition and physical properties of K_xWO_3 superconducting thin films.

II. EXPERIMENT

K-doped WO_3 films are synthesized in a pulse laser deposition (PLD) system, with K_xWO_3 targets prepared by spark plasma sintering, a technique reviewed recently in a viewpoint set [14]. We chose K concentration of $x = 0.33$ for the target because beyond this doping the hexagonal structure is unstable. The bulk T_c at this composition is $\sim$2–2.5 K. The thin films were deposited under O_2 pressure of $P(O_2) =$ 10–100 mtorr and substrate temperatures ranging from

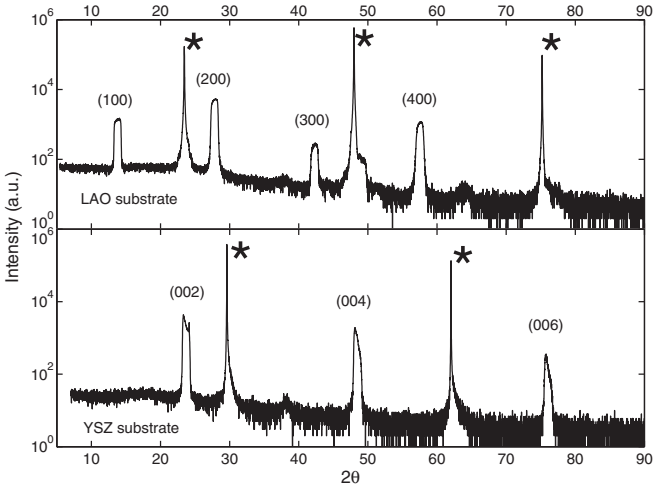

FIG. 1. X-ray diffraction (XRD) curves for K_xWO_3 on LAO (100) and YSZ(111) substrates. In both figures, substrate peaks are denoted with a star.

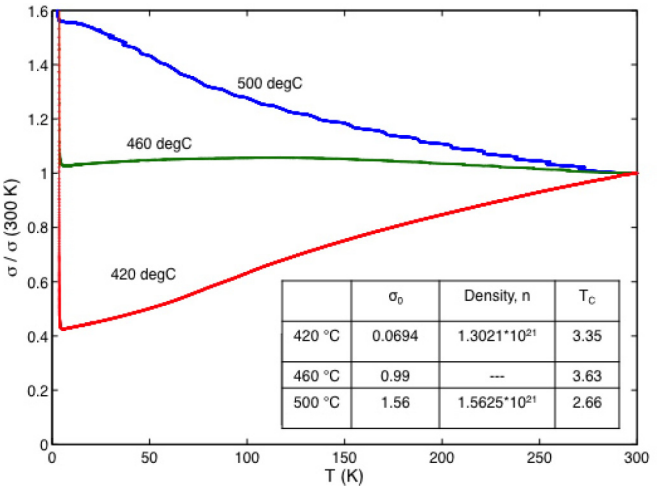

FIG. 2. (Color online) Normalized conductivity vs temperature for three 250-nm-thick $K_{0.33}WO_{3-y}$ films on YSZ substrates. The films are annealed in vacuum at different temperatures, with properties shown in the inset table. The units of T_{anneal} are degrees Celcius, σ_0 is given in $1/\text{m}\Omega\text{cm}$, n in $/\text{cm}^3$, and T_c in degrees Kelvin. The conductivity at zero temperature, σ_0, is found by extrapolating to zero temperature. Density n, for the 460-°C sample was not measured. Note that the high-T_{anneal} sample displays metalliclike temperature dependence, while the lowest-T_{anneal} sample has an insulatorlike temperature dependence. The T_c of the metalliclike film, when compared to the other two, is lower.

$T_{\text{sub}} = 300$–$600\,^\circ$C. The laser was pulsed at 4 Hz and the substrate to target distance was fixed at 4 cm. We found that films grown at substrate temperatures less than 500 °C were insulating (with MΩ or larger resistance). Films grown at 500–600 °C were superconducting, but the superconducting films produced in this way exhibited varying transport characteristics, with the sign of $d\rho/dT$ varying uncontrollably. We attribute this variability to a nonzero y in $K_{0.33}WO_{3-y}$. $LaAlO_3$ (LAO) (100) and Y-ZrO_2 (YSZ) (111) were utilized as substrates, with a- and c-axis oriented hexagonal films obtained on LAO and YSZ substrates, respectively, see Fig. 1 [15]. On a-axis oriented LAO, $a \sim 7.39$ Å, and on c-axis oriented YSZ, $c \sim 7.614$ Å. Due to the inherent twin domains of LAO, two domains were seen for a-axis oriented $K_{0.33}WO_3$ films on LAO, corresponding to [001] film growth on either [100] LAO or [010] LAO.

By trial and error, we found a two-step deposition procedure that yielded reproducible results. In the first step, insulating films were deposited at $T_{\text{sub}} = 450$–$480\,^\circ$C at $P(O_2) = 100$ mtorr. Then, a 30-min post-deposition vacuum anneal step was performed at various annealing temperatures T_{anneal}. This post-deposition procedure enabled us to obtain reliable and controllable film characteristics that varied systematically with T_{anneal}. An example is as shown in Fig. 2 and the associated inset. The films are 250-nm-thick, with higher annealing temperatures corresponding to more oxygen deficient films (i.e., larger y). These films display higher conductivity, with the low temperature Hall effect showing larger carrier densities in the high-T_{anneal} samples. We note that the temperature dependence of the normal state for the high-T_{anneal} sample is metallic $d\rho/dT > 0$, while that of the lower temperatures is insulating, $d\rho/dT < 0$. Note also that all three films display anomalous inflections in the resistivity at higher temperature, similar to what is observed in bulk crystals.

III. RESULTS AND DISCUSSION

From the magnetic field dependence of the resistive transition, we extract the critical field H_{c2} for the 250-nm-thick metallic, intermediate and insulating films grown on YSZ shown in Fig. 2. H_{c2} is defined by the 50% criterion, taking the field where the resistivity is at half that of the normal state. For all three films, H_{c2} is larger when the field is applied parallel to the c axis, see Fig. 3. Similar anisotropy is found in films of comparable thickness grown on LAO, suggesting this is an intrinsic property of the films. This anisotropy is qualitatively consistent with band structure calculations that reveal wide one-dimensional bands and narrow three-dimensional bands, with the 1D band responsible for the metallic character along the c axis [13]. The anomalous kink at high temperatures in these films is also consistent with the thought that either structural or electronic instabilities exist along the c axis and compete with the superconductivity in the K- and Rb-doped WO_3.

To further examine the possible competing effects of structural or CDW instabilities and superconductivity for a given alkali concentration, we next investigated the thickness dependence of the film properties at fixed T_{anneal}. We focus on KWO_3 on LAO substrates, where the c axis is parallel to sample surface, so that tuning the thickness does not directly affect the transport along the c axis. A two-step deposition procedure was utilized as before, with the film thickness set by changing the material deposition time. A 30-minute post-deposition annealing step with $T_{\text{anneal}} = 500\,^\circ$C was done for all samples. The sample thickness d ranges from 250 nm for the thickest film to 10 nm for the thinnest. As shown by the scanning electron microscopy (SEM) images in Fig. 4, the topology of the films depends on film thickness, with a major break around $d = 30$ nm.

Several notable features are observed in the transport measurements. The sheet resistance R_s of our films increases

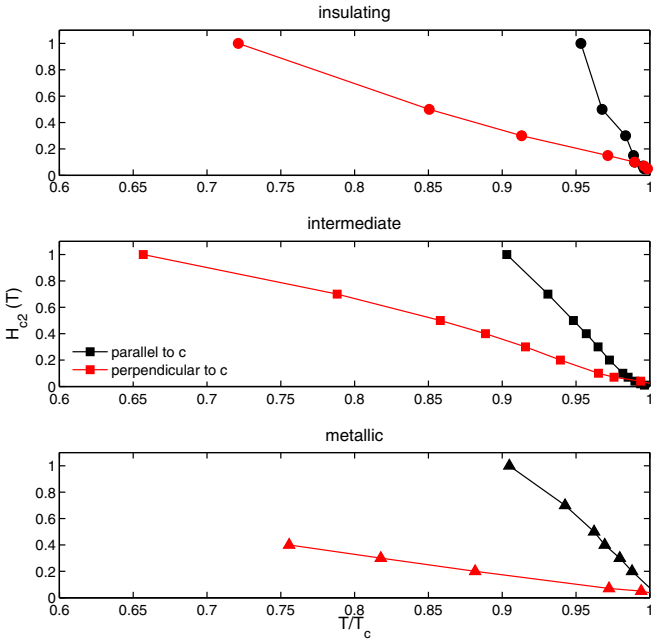

FIG. 3. (Color online) H_{c2} vs T/T_c for the insulating, intermediate, and metallic superconducting films shown in Fig. 2. H_{c2} is defined via the 50% criterion. Black curves denote measurements where the field is parallel to c axis, and red curves are for the case with field perpendicular to the c axis. All three films have thickness 250 nm.

by over five decades when the film thickness is reduced from 250 nm to 10 nm, as shown in Fig. 5. Films thicker than 50 nm have a clear superconducting transition (zero-resistance transition) near ∼3 K, while both the 40-nm and 30-nm films show an onset transition at low temperature, though no zero resistance state down to 2 K, the lower temperature

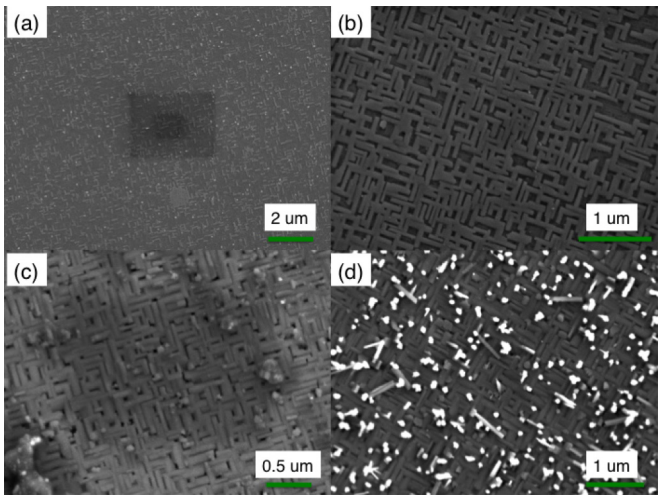

FIG. 4. (Color online) Scanning electron microscope image of (a) 10-nm (2-μm scale bar), (b) 30-nm (1-μm scale bar), (c) 100-nm (0.5-μm scale bar), and (d) 250-nm (1-μm scale bar) films. With longer deposition time, the average thickness increases and the rodlike crystallites also more densely cover the substrate surface. The square dark regions in (a) and (c) are due to damage from imaging the region at high magnification.

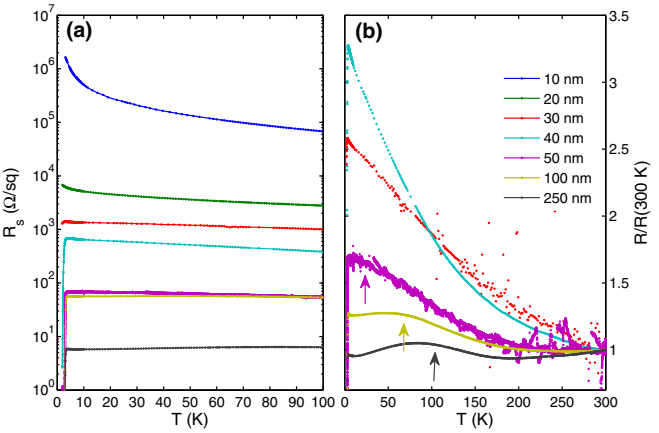

FIG. 5. (Color online) (a) Sheet resistance vs temperature for $K_{0.33}WO_3$ thin films on LAO substrate. As the thickness is reduced, the films undergo a superconductor to insulator transition. (b) R scaled by R(300 K) is shown as a function of temperature. Note the unusual temperature dependence for the 250-nm, 100-nm, and 50-nm films. The characteristic temperature of the anomaly, marked by arrows, is suppressed with reduced film thickness.

limit of our PPMS cryostat. At $d = 10$ nm, the film exhibits insulating-like behavior down to 2 K. In the normal state, a resistive anomaly at high temperatures, similar to features seen in bulk KWO_3 and in the films grown on YSZ substrates, is visible in the three thickest films from 250 to 50 nm, Fig. 5(b) (marked with arrows). The characteristic temperature of the anomaly is progressively reduced as the thickness is reduced and is no longer present in films thinner than 50 nm, all of which show insulating normal state temperature dependence. At present, we do not fully understand this behavior, but we may speculate on some possibilities. If the anomaly is due to structural distortion, then perhaps the strain from the substrate is preventing the distortion. However, XRD results show that the lattice parameters do not change significantly with thickness, suggesting that there is little strain effect taking place. Alternatively, if the anomaly has electronic origin, such as from CDW [13,16], then perhaps the lower dimensionality in the ab plane of the thinner films is preventing the CDW transition.

The SEM images provide a microscopic explanation for the large change in sheet resistance. The KWO_3 forms rodlike crystallites on the substrate surface, which interconnect with one another in the thicker films. Resistivity and Hall measurements at 100 K give $k_F l \sim 10$ for the 250-nm film, where k_F is the Fermi wave number and l is the mean free path. As d is reduced, a major break is observed around $d = 30$ nm ($k_F l \sim 0.6$), with the film breaking up into regions of less connected crystallites. Transport measurements show insulating temperature dependence and significantly reduced T_c, see Fig. 6 where we plot T_c, resistivity and residual resistivity ratio $[RRR = \rho(300K)/\rho_0]$ versus ln(d). ρ_0 is defined by extrapolating the resistivity to $T = 0$. The majority of the rodlike crystallites have lateral dimensions longer than the superconducting coherence length, $\xi \sim 6$–10 nm (extracted from magnetic field dependence of the resistive transition for thick 250-nm films). Despite this, in the thinnest film with $d = 10$ nm [Fig. 4(a)], the combination of reduced thickness

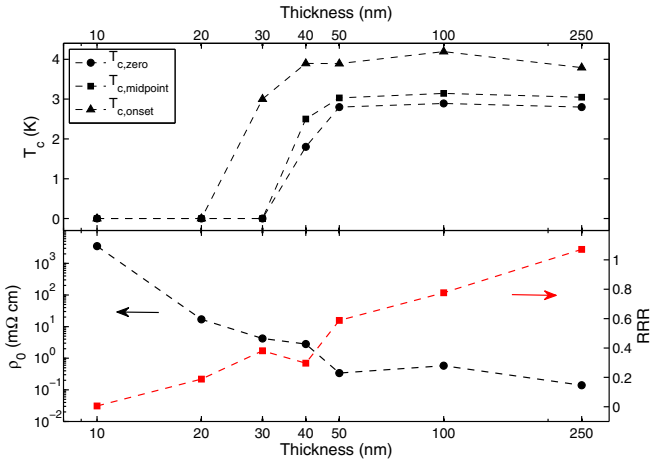

FIG. 6. (Color online) (Top) T_c (zero, midpoint, and onset) vs thickness (logarithmic scale) for the $K_{0.33}WO_3$ films shown in Fig. 5. The midpoint and zero T_c for the 30-nm film could not be determined due to cryostat limitations. (Bottom) ρ_0 at $T = 0$ and $RRR = \rho(300K)/\rho_0$ as a function of d (log-log scale). Dashed lines in both panels are guide to the eye. Note that ρ_0 is relatively constant in the thick films, concurrently, $T_{c,\mathrm{onset}}$ remains relatively constant.

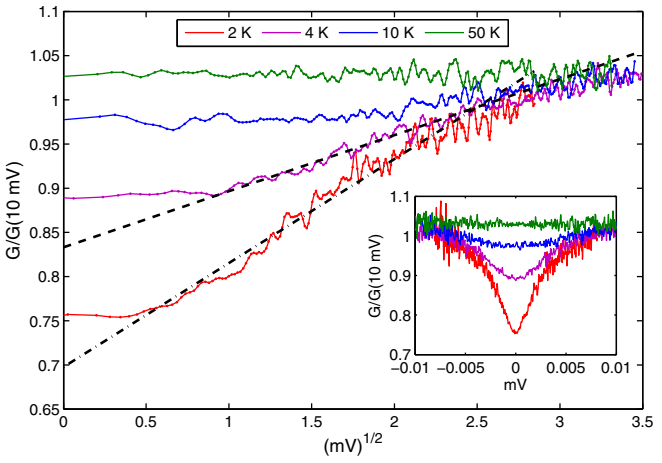

FIG. 7. (Color online) Normalized conductance vs $(\mathrm{mV})^{1/2}$ for the 250-nm-thick $K_{0.33}WO_3$ film shown in Fig. 5. A clear suppression in the density of states at zero bias is observed. The linear fits to the 4-K (dashed) and 2-K (dot-dash) data allow the extraction of bounds on the correlation gap Δ and normalized density of states at zero temperature N(0); for the correlation gap, which is related to the slope, 35 meV $< \Delta <$ 172 meV and the y intercept gives the normalized density of states at zero temperature, $0.7 < N(0) < 0.83$.

and connectedness lead to a macroscopically insulating film and $k_F l \sim 0.1$.

The resistive anomaly in the thicker films suggests that disorder induced increased Coulomb interactions are present. To further investigate, we performed point contact spectroscopy (PCS) measurements on the 250-nm and 100-nm films, which both display noticeable anomalies and $k_F l \sim 10$ and 5, respectively. Differential conductance measurements were obtained in a home built PCS setup, with the point contact junction formed by pressing an aluminum tip onto the film surface. In Fig. 7, we show the normalized conductance plotted versus the square root of bias voltage in mV for the 250-nm film. A cusp is seen in the differential conductance tunneling measurements (Fig. 7 inset), reminiscent of the cusp seen in Nb:Si, which is a well-known system with disorder driven metal-insulator transition [17]. We extracted the zero-temperature normalized density of states and correlation gap from McMillan's theory, $N(E) = N(0)[1 + (E/\Delta)^{1/2}]$ [18], where $N(0)$ is the normalized density of states at zero temperature, E is the bias voltage, and Δ is the correlation gap. The dashed (4 K) and dot-dash (2 K) fits in Fig. 6 allow to extract $0.7 < N(0) < 0.83$ and 35 meV $< \Delta <$ 172 meV within this temperature range. Similarly, we find for the 100-nm film $N(0) = 0.2$ and $\Delta = 3.2$ meV at 5 K. These results demonstrate that the films are indeed 3D disordered superconductors.

The fact that superconductivity persists despite the disorder points to the crucial role in this material system of strong electron-phonon coupling to superconductivity. To get a sense of the strength of the electron-phonon coupling, we utilize the theory of Belitz relating T_c degradation to the correlation gap [19]. A similar analysis was performed to account for the difference in transition temperatures for the lead- and potassium-doped Bismuthate superconductors [20]. Following the analysis of Ref. [20], we calculate T_c with the following formula:

$$T_c = \frac{\Theta}{1.45} \exp\left\{\frac{-1.04(1+\tilde{\lambda}+Y')}{\tilde{\lambda}+\tilde{\mu}^*[1+0.62\tilde{\lambda}/(1+Y')]}\right\}, \qquad (1)$$

where Θ is the Debye temperature, $\tilde{\lambda}$ is the disorder dependent electron-phonon coupling, $\tilde{\mu}^*$ the disorder dependent Coulomb pseudopotential, and $Y' \approx 1/N(0) - 1$ is the disorder parameter, which can be directly related to the normalized tunneling density of states. At zero disorder, Eq. (1) is McMillan's T_c formula. We have calculated the T_c for the

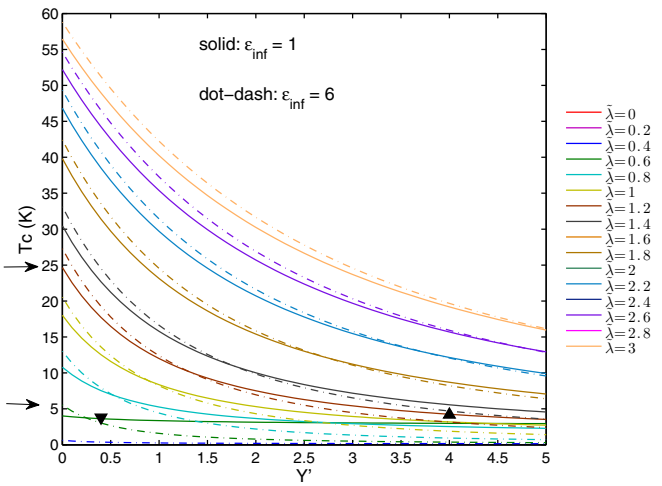

FIG. 8. (Color online) T_c vs Y' using Eq. (1) {Eq. (7) from Ref. [19]}. Down triangle marks the data for the 250-nm film ($Y' = 0.4$, $T_{c,\mathrm{onset}} = 3.79$ K) shown in Fig. 6 and the up triangle marks the 100-nm film ($Y' = 4$, $T_{c,\mathrm{onset}} = 4.19$ K). The pinpointed curves correspond to $\tilde{\lambda} = 0.6$ (250-nm film) and $\tilde{\lambda} = 1.2$ (100-nm film). Note the disorder free $T_{c,0} = 25$ K for the 100-nm film (top arrow).

KWO_3 films, see Fig. 8, assuming $\Theta = 415$ K, similar to what is experimentally found for $RbWO_3$ [21]. In addition, we have followed Kitazawa [22] in calculating the disorder free Coulomb parameter $\mu = 0.3$–0.44 and the disorder free effective Coulomb repulsion coefficient $\mu^* = 0.13$–0.153 [23] from the electron density n, dielectric constant ϵ, and Fermi energy E_F [24]. The range here is due to the maximum and minimum value for ϵ: $\epsilon = 6$ for $k \to 0$ and $\epsilon = 1$ for $k \to \infty$.

Utilizing experimental data points $T_{c,\text{onset}} = 3.79$ K and $Y' = 0.4$ for the 250-nm film and $T_{c,\text{onset}} = 4.19$ K and $Y' = 4$ for the 100-nm film, we can read off the values $\tilde{\lambda} = 0.6$ for the 250-nm film and $\tilde{\lambda} = 1.2$ for the 100-nm film. Thus despite the strong disorder ($Y' = 4$ for the 100-nm film), the electron-phonon coupling is large, and hence, superconductivity is still observed. Interestingly, if we back out the disorder free superconducting transition $T_{c,0}$, we find it is nearly 25 K for the 100-nm film, nearly six times the actual T_c. Although a substantial increase, it is still well short of the reported high-T_c anomalies in other tungsten bronzes. Clearly then, the mechanism presented here is insufficient to account for the rather high-T_c anomalies observed the Na- and H-doped tungsten bronzes.

IV. CONCLUSION

We present the first thin film study of K-doped WO_3 superconductors. Via a two-step deposition and post-annealing procedure, films with reproducible transport properties are obtained. Reducing the film thickness results in a disorder driven superconductor to insulator transition. Analysis of point contact spectroscopy data with Belitz's disordered superconductor formalism suggests that the thicker bulklike films exhibit strong electron-phonon coupling in the presence of disorder. Extrapolating to the case of zero disorder results in a rather high disorder free $T_{c,0} \sim 25$ K (for the 100-nm film). Understanding microscopically and locally the reasons for disorder in these films will be valuable in providing direction for reproducing and searching for the high-T_c anomalies observed in the Na- and H-doped WO_3.

ACKNOWLEDGMENTS

This work supported by an AFOSR under DoD MURI Grant FA9550-09-1-0583.

[1] S. Reich, G. Leitus, R. Popovitz-Biro, A. Goldbourt, and S. Vega, J. Supercond. Novel Magn. **22**, 343 (2009).
[2] S. Reich, G. Leitus, Y. Tssaba, Y. Levi, A. Sharoni, and O. Millo, J. Supercond. Novel Magn. **13**, 855 (2000).
[3] A. E. Aliev, Supercond. Sci. Technol. **21**, 115022 (2008).
[4] E. Berg, D. Orgad, and S. A. Kivelson, Phys. Rev. B **78**, 094509 (2008).
[5] V. L. Ginzburg, Phys. Scr. **T27**, 76 (1989).
[6] C. J. Raub, A. R. Sweedler, M. A. Jensen, S. Broadston, and B. T. Matthias, Phys. Rev. Lett. **13**, 746 (1964).
[7] M. R. Skokan, W. G. Moulton, and R. C. Morris, Phys. Rev. B **20**, 3670 (1979).
[8] R. K. Stanley, R. C. Morris, and W. G. Moulton, Phys. Rev. B **20**, 1903 (1979).
[9] L. C. Ting, H. H. Hsieh, H. H. Kang, D. C. Ling, H. L. Liu, W. F. Pong, F. Z. Chien, and P. H. Hor, J. Supercond. Novel Magn. **20**, 249 (2007).
[10] L. H. Cadwell, R. C. Morris, and W. G. Moulton, Phys. Rev. B **23**, 2219 (1981).
[11] R. Brusetti, P. Bordet, J. Bossy, H. Schober, and S. Eibl, Phys. Rev. B **76**, 174511 (2007).
[12] R. Brusetti, P. Haen, and J. Marcus, Phys. Rev. B **65**, 144528 (2002).
[13] K.-S. Lee, D.-K. Seo, and M.-H. Whangbo, J. Am. Chem. Soc. **119**, 4043 (1997).
[14] Subhash H. Risbud and Young-Hwan Han, Scr. Mater. **69**, 105 (2013).
[15] K. Munakata, Ph.D. thesis, Stanford University, 2012.
[16] S. Raj, T. Sato, S. Souma, T. Takahashi, D. D. Sarma, P. Mahadevan, J. C. Campuzano, M. Greenblatt, and W. H. McCarroll, Phys. Rev. B **77**, 245120 (2008).
[17] G. Hertel, D. J. Bishop, E. G. Spencer, J. M. Rowell, and R. C. Dynes, Phys. Rev. Lett. **50**, 743 (1983).
[18] W. L. McMillan, Phys. Rev. B **24**, 2739 (1981).
[19] D. Belitz, Phys. Rev. B **40**, 111 (1989).
[20] K. Luna, P. Giraldo-Gallo, T. Geballe, I. Fisher, and M. Beasley, arXiv:1311.4212v1.
[21] A. J. Bevolo, H. R. Shanks, P. H. Sidles, and G. C. Danielson, Phys. Rev. B **9**, 3220 (1974).
[22] K. Kitazawa, M. Naito, T. Itoh, and S. Tanaka, J. Phys. Soc. Jpn. **54**, 2682 (1985).
[23] P. Morel and P. W. Anderson, Phys. Rev. **125**, 1263 (1962).
[24] B. Ingham, S. C. Hendy, S. V. Chong, and J. L. Tallon, Phys. Rev. B **72**, 075109 (2005).